Cumhuriyet Sci. J., 43(2) (2022) 346-350
DOI: https://doi.org/10.17776/csj.1104315

Cumhuriyet Science Journal

| csj.cumhuriyet.edu.tr | Founded: 2002 ISSN: 2587-2680 e-ISSN: 2587-246X Publisher: Sivas Cumhuriyet University

Influence of the Core Pillar Height on the Bandgap Characteristics of Piezoelectric Phononic Crystals with Ring-Shaped Grooves

Furkan Kuruoğlu [1,a,*]

[1] *Department of Physics, Faculty of Science, Istanbul University, Vezneciler 34134, Istanbul, Turkey.*
**Corresponding author*

Research Article

History
Received: 16/04/2022
Accepted: 16/06/2022

Copyright
©2022 Faculty of Science, Sivas Cumhuriyet University

ABSTRACT

Dispersion profiles and surface acoustic wave attenuation characteristics of ring-shaped phononic crystals are investigated as a function of the core pillar height. Finite element method simulations are carried out for both band analyses and transmission spectra calculations. The results reveal that the increase at the core pillar height leads to a decrement in the local resonance band gap frequencies and the corresponding transmission peaks. The obtained dispersion profiles show that the phononic crystal bandgap also expands from 6 MHz to 11 MHz while the pillar height increases from 5 μm to 7 μm. Similar characteristics are also seen in the transmission spectra for the varying core pillar heights of the ring-shaped periodic grooves. In addition, surface acoustic wave attenuation competency depends on the core pillar height. The resonant frequency of the phononic crystals can be tuned by adjusting the core pillar height.

Keywords: Surface acoustic wave, Phononic crystal, Finite element method, Phononic bandgap.

[a] *furkan.kuruoglu@istanbul.edu.tr* *https://orcid.org/0000-0002-5314-4441*

Introduction

It has always been desired to sense and manipulate biological or inorganic objects by not only harmless but also contactless methods. Using light and acoustic waves [1] is the most practical way to reach this aim. Surface acoustic waves (SAWs) have been receiving extensive attention on various research and application areas related to delay lines [2], filters [3, 4], microfluidics [5–7], gas-detection [8, 9], mass detection [10] and bio-detection applications [11, 12]. Due to these wide ranges of research and application areas, SAW devices have drawn significant interest in recent decades.

By the proposition of the phononic crystals (PnCs)[13], which offer acoustic band gaps depending on the periodicity and geometry of the material, the guided SAWs have also been enabled, similar to photonic crystal slabs [14–16]. Recently, a periodic array of pillars emerged as the prominent phononic crystal geometry with a considerably broad range of application areas[17–19].

Piezoelectric phononic crystals (PPnCs), periodic elastic structures composed of either extrusions or grooves on a piezoelectric substrate, have also been drawing attention in terms of both physical properties and applications. Applications of PPnCs have emerged in different fields such as waveguiding [20–22], bio and mass sensing [23–25], energy harvesting [26] and microfluidics [27]. Fundamentally, the locally resonant and/or the Bragg bandgap of PPnCs paves the way for various types of applications and the bandgap characteristics are closely related to the geometric parameters of the PPnC.

Ash et al. showed that broader SAW band gaps could be achievable by using ring-shaped metamaterials as being piezoelectric phononic crystals [28]. Also, the geometrical parameters like ring radii, pillar height and groove depth can tune the frequency range where the phononic crystal will be efficient. Because of these reasons, it is crucial to obtain the proper geometrical parameters and the effects on the acoustic bandgap for superior phononic device applications.

In this work, band profile of PPnC and SAW attenuation characteristics are simulated by means of the finite element method (FEM) for the ring-shaped groove model. Simulations are performed for various pillar heights, which differ from the groove height, while the inner and outer ring radii have fixed values.

Material and Method

FEM simulations were performed to inspect the band structures of the ring-shaped PPnCs and SAW transmission spectra as a function of the PPnC pillar height. All simulations were carried out through COMSOL Multiphysics 5.3a by employing the piezoelectricity module, which couples the elastic wave equation and relevant Maxwell's equation (Gauss' law) to obtain stresses and electrical potential distributions over piezoelectric materials.

For ease of comparison to the work of Ash et al. [19], a two-dimensional (2D) PPnC in the square lattice is considered. As shown in Figure 1a), the square PPnCs are modeled by fixing the groove depth (h_{grv}) to 6 μm, groove top radius (r_o) to 5 μm, pillar bottom radius (r_i) to 3 μm, lattice constant (a) to 12 μm, while the pillar height (h_{pillar}) is ranged from 5 μm to 7 μm. The wall inclination angle (θ)

is set as 10.2°, which is experimentally reported for 128° Y-cut X-propagating (YX-128°) lithium niobate ($LiNbO_3$) [29]. This cut is defined in COMSOL through the Euler angles (α,β,γ)=(0,38°,0). The definition of Euler angles is more convenient than the transformation of elasticity and coupling matrices of Z-cut $LiNbO_3$.

The eigenfrequencies are determined on the irreducible Brillouin zone (BZ) in the 1st BZ and the wavevector **k** is swept on the boundaries along the $\Gamma \rightarrow X \rightarrow M \rightarrow \Gamma$ path for the square array. Figure 1b represents the 3D schematic of the modeled PPnC unit cell. Bloch-Floquet periodic boundary condition (PBC) is defined for both opposing sides of the unit cell and the bottom side of the unit cell was defined as a fixed constraint surface to avoid unwanted displacement effects. The piezoelectric slab height was chosen as h_{slab}=200 μm, a value much higher than SAW penetration depth at the frequency range of interest (around 100 MHz). According to the geometric parameters of the PPnC unit cell given in Figure 1, there is a local resonance band gap (LRBG) resulting from the resonance vibrations of the core column, which is found to be below the expected Bragg band gap [19]. Here, it is shown that the characteristics, i.e., the LRBG edge frequencies and width can be tuned by varying h_{pillar}.

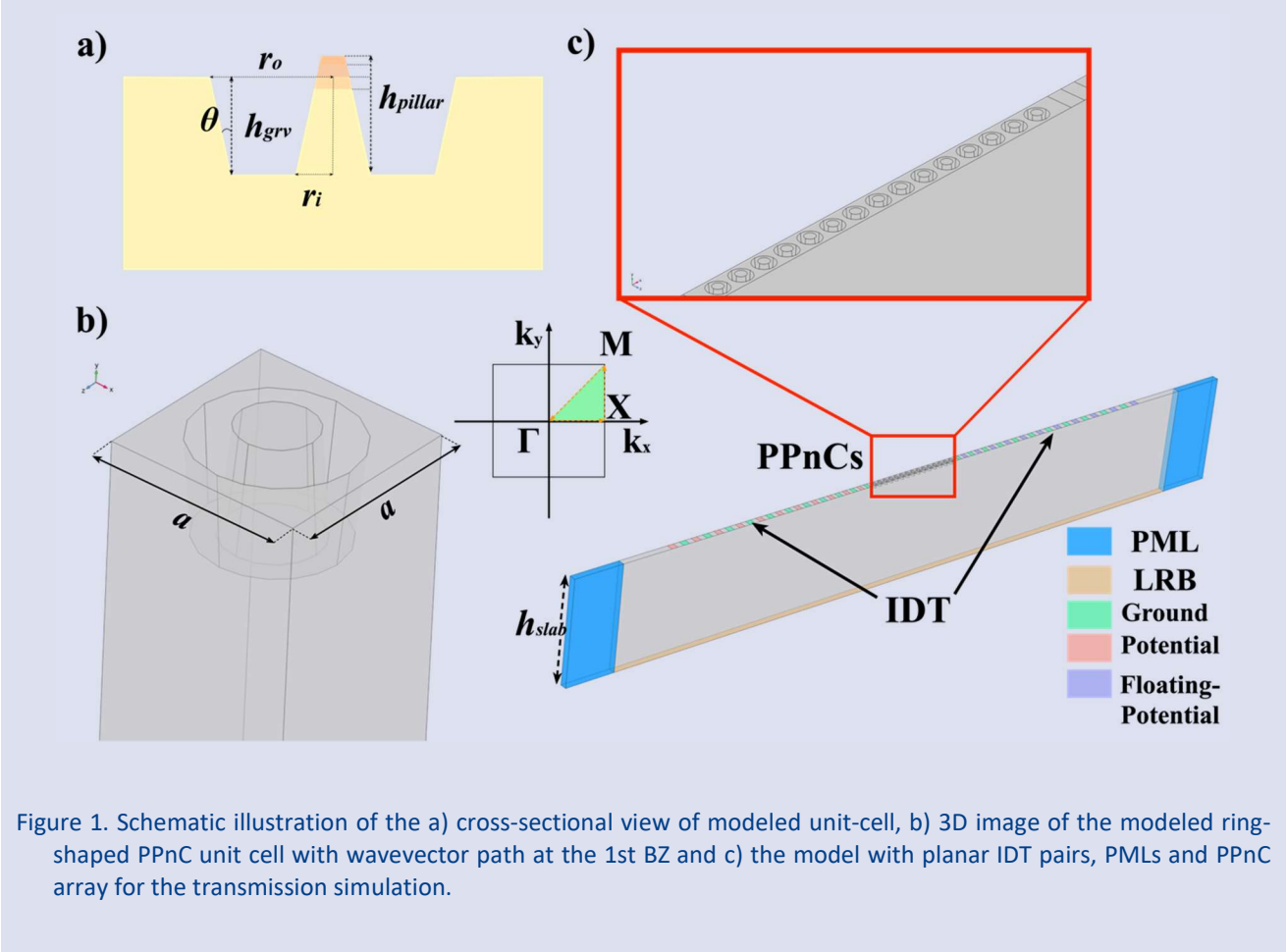


Figure 1. Schematic illustration of the a) cross-sectional view of modeled unit-cell, b) 3D image of the modeled ring-shaped PPnC unit cell with wavevector path at the 1st BZ and c) the model with planar IDT pairs, PMLs and PPnC array for the transmission simulation.

After the PPnC band structure is obtained for each h_{pillar} value, the corresponding transmission spectra are obtained through frequency domain FEM simulations. Here, Rayleigh-type SAWs are generated by interdigitated transducers (IDTs), which are the standard means of radio frequency (RF) SAW generation in such systems [30]. SAW transmission spectra are simulated for two facing identical IDTs and a PPnC array in between, as shown in Figure 1(c). To work in a broad frequency range, chirped IDTs [31] are modeled, where the finger width ranges from 7.5 μm to 12.5 μm with a step increase of $\Delta\omega$=0.5 μm and the number of finger pairs in each IDT is N=11. The PPnC array with 15 periodic units equally spaced from the IDT fingers lays along [10] direction. The IDT on the left in Figure 1(c) is defined as the source to propagate SAW, while the right-side one is used to probe the transmitted signal through the floating potential (V_{probe}). SAW transmittance (S_{21}) is calculated from the $S_{21} = 20 \times log_{10}(V_{probe}/V_0)$ where V_0 = 50 V is the RF amplitude. Perfectly matched layers (PML) [32] are placed at the edge of the model in the direction of the SAW propagation and the bottom side was defined as a low-reflecting boundary (LRB) to minimize the unwanted reflections. PBC is used on the sides parallel to the SAW propagation direction, that is only one row of the PPnC is modeled, while the infinitely-many rest images are replicates through the PBC.

Results and Discussion

.

The band structure of the PPnC is plotted as a function of pillar height inFigure 2. The red dashed lines show the Rayleigh SAW modes of the unperturbed bulk and the other leaky SAW dispersion lines are not presented. The grey shaded areas denote the ranges of these leaky modes, which are ruled out. Below the SAW line in Figure 2, there appear several bands due to different vibration mechanisms. The lowermost two bands correspond to bending and expansion modes of the core pillar therefore flat they are [19]. The third band, on the other hand, comprises of anti-resonant modes of the outer grooves. The orange stripes lying between the second and third bands are the LRBGs, which appear between 105.2 - 111.2 MHz for the 5 μm core pillar height and shift towards the frequencies between the 70.8-82.4 MHz while the core pillar height increases up to 7 μm. Only one LRBG appears for each case, where the Bragg bandgap frequency is estimated to be around 200 MHz, from the condition $\alpha/\lambda=1/2$.

The two bands below the LRBG related to the pillar modes shift to lower frequencies by the increasing pillar height of the ring-shaped PPnC. Similar results were reported for the pillar type PPnC arrays, through both experimental and simulation results [17, 19, 33]. Besides, the gap between the dispersion lines corresponds to the localized modes of the pillar decreases with the increasing height.

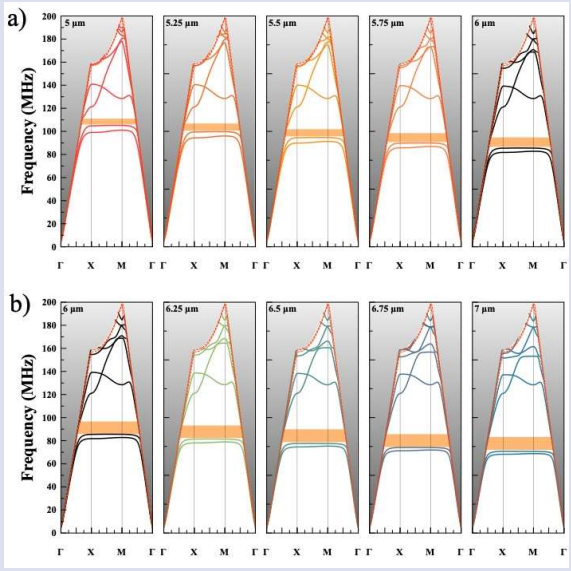


Figure 2. The band structures of the square array ring-shaped PPnCs with different pillar heights: a) 5 μm to 6 μm and b) 6 μm to 7 μm.

This pillar height dependence of the local resonant frequency also paves the way for the adjustment of the frequency, likewise the previous reports for the all-pillar type PPnCs, which is defined to be located above the surface of substrate [19]. Differently from the all-pillar PPnC arrays, for the ring-shaped PPnCs, the third band at the higher frequencies can be modulated by varying the pillar height of the ring-shaped PPnCs.

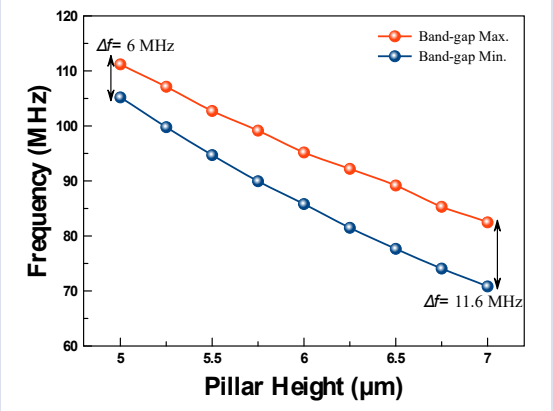


Figure 3. Variation of LRBG edge frequencies as a function of the PPnC pillar height.

Figure 3 shows the bandgap change as a function of the pillar height of the ring-shaped PPnCs. As seen in Figure 3, the LRBG location shifts towards lower frequency regions. At the same time, the bandgap expands nearly by a factor of 2 from the lowest (5 μm) to the highest (7 μm) pillar height. The monotonic behavior may be attributed to the added mass with increasing h_{pillar}, which results in elevated inertia of the core pillars.

The transmission spectra (S_{21}) are obtained for a better understanding of PPnC and SAW interaction. Figure 4 shows the SAW transmission spectra ranged between 70 MHz and 130 MHz for each pillar heights from 5 μm to 7 μm. The red dashed line in Figure 4 represents the S_{21} spectrum of the bare chirped IDT pairs (i.e., without PPnC in between). Each transmission spectrum has two apparent peaks and the major one is located at nearly 100 MHz, while the minor one is around 80 MHz. As compared to the dispersion profiles, both S_{21} peaks shift towards lower frequencies until the pillar top is in line with the $LiNbO_3$ surface (i.e., h_{pillar}=6 μm). Just after the pillar reaches above the surface, the peak around the 100 MHz slightly shifts to higher frequencies, whereas the minor peak continues to shift towards lower frequencies. The characteristics of the minor peak can be attributed to pillar height dependency of the local resonant profile of the ring-shaped PPnC [18].

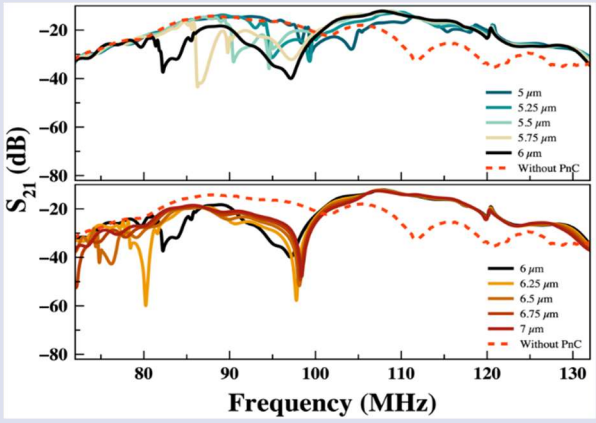


Figure 4. SAW transmission spectra of ring-shaped square PPnC array on the [10] orientation for different pillar heights

A drastic increment is also observed in the SAW attenuation (transmission loss) for $h_{pillar}>h_{grv}$ in both major and minor peaks, as shown in Figure 5. For $h_{pillar}\geq 6.25$ μm, however, transmission loss shows a decreasing profile with the increment of the pillar height of the PPnC, Figure 5(b).

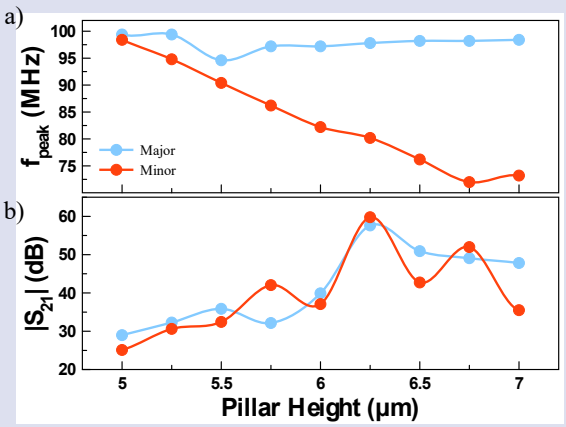


Figure 7. a) Major and minor peak frequencies in S21 spectra and, b) the attenuation intensity at the peak frequency for the various pillar height of the ring-shaped PPnC arrays.

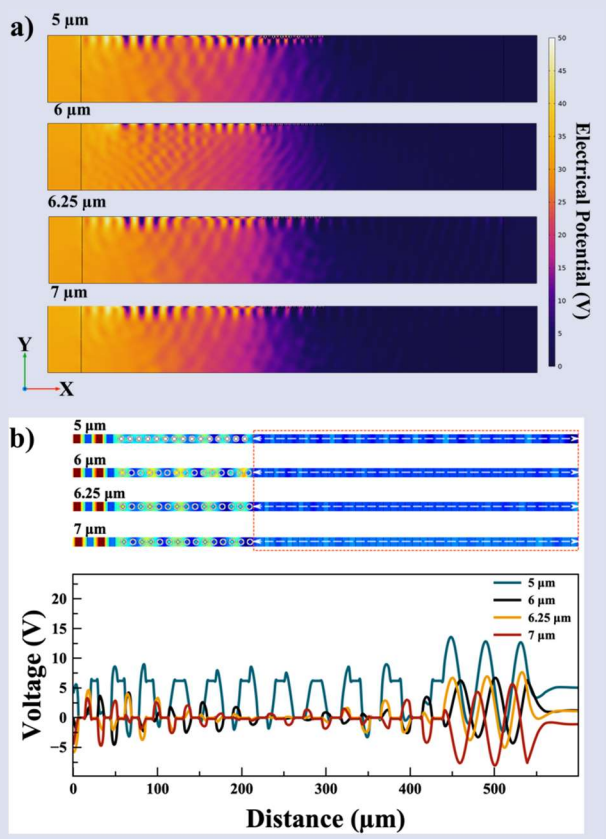


Figure 6. a) Cross-sectional view of the electrical potential distribution for different ring-shaped PPnC pillar heights calculated at the corresponding S_{21} major peak frequencies (99.4 MHz, 97.2 MHz, 97.8 MHz and 98.4 MHz, respectively). b) Electrical potential distribution on the slab surface and the line profile voltage distribution on the probe IDT for the various core pillar height.

Figure 6 visualizes the potential distribution over the simulated model at the major peak frequencies corresponding to different h_{pillar} values extracted from the SAW transmission spectra in Figure 4. It can be clearly seen in Figure 6 that PPnC arrays with lower height pillars ($h_{pillar}<h_{grv}$) have no superior attenuation performance. In good agreement with the results in Figure 4, the PPnC arrays that have pillars with $h_{pillar}\geq h_{grv}$, exhibit better attenuation characteristics according to the more pronounced darker regions in Figure 6a and the voltage distributions in the Figure 6b.

Conclusion

In summary, the band structures and the SAW transmission spectra of PPnCs with ring-shaped grooves are simulated as a function of core pillar height. It is observed that the increment in the pillar height of the ring-shaped PPnC leads to a decrease in the LRBG edge frequencies while the width of LRBG is increasing. Agreeing results are obtained from the SAW transmission peaks and the voltage distribution on the probe IDT, which tend to show decreasing attenuation profile with the increasing pillar height. The potential distributions also show the ring-shaped PPnCs with $h_{pillar}\geq$ 6 μm have better attenuation performance.

Taking into account all of these findings from the simulations, the frequencies at which the ring-shaped PPnCs are functional can be utilized to tune surface acoustic wave attenuation by adjusting the pillar height of the model. Increasing pillar height is equivalent to adding extra load on the pillars. Thus, the investigated PPnC can be employed in sensing applications through the mass loading effect.

Acknowledgment

I appreciate support from Prof. Dr. Ahmet Cicek and Prof. Dr. Ayse Erol for their valuable discussion on the results. The work is funded by The Scientific and Technological Research Council of Turkey (TUBITAK) (Project No: 120F337).

Conflicts of interest

The author states that did not have a conflict of interests.

References

[1] Collins D.J., Devendran C., Ma Z., Ng, J.W., Neild A., Ai Y., Acoustic tweezers via sub–time-of-flight regime surface acoustic waves, *Sci. Adv.*, 2 (7) (2016) e1600089.

[2] Topaltzikis D., Wielunski M., Hörner A.L., Küß M., Reiner A., Grünwald T., Schreck M., Wixforth A., Rühm W., Detection of x rays by a surface acoustic delay line in contact with a diamond crystal, *Appl. Phys. Lett.*, 118 (13) (2021) 133501.

[3] Su R., Shen J., Lu Z., Xu H., Niu Q., Xu Z., Zeng F., Song C., Wang W., Fu S., Pan F., Wideband and Low-Loss Surface Acoustic Wave Filter Based on 15° YX-$LiNbO_3$/SiO_2/Si Structure, *IEEE Electr. Device L.*, 42 (3) (2021) 438-441.

[4] Su R., Fu S., Shen J., Lu Z., Xu H., Yang M., Zeng F., Song C., Wang W., Pan F., Power Durability Enhancement and Failure Analysis of TC-SAW Filter With Ti/Cu/Ti/Cu/Ti Electrodes, *IEEE T. Device Mat. Re.*, 21 (3) (2021) 365-371.

[5] Xie Y., Mao Z., Bachman H., Li P., Zhang P., Ren L., Wu M., Huang T.J., Acoustic Cell Separation Based On Biophysical Properties*., J. Biomechanical Eng*., 142 (3) (2020) 031005-1-9

[6] Qian J., Ren J., Liu Y., Lam R.H.W., Lee J.E.-Y., A two-chip acoustofluidic particle manipulation platform with a detachable and reusable surface acoustic wave device, *Analyst*, 145 (23) (2020) 7752-7758.

[7] Agostini M., Greco G., Cecchini M., Full-SAW Microfluidics-Based Lab-on-a-Chip for Biosensing, *IEEE Access*, 7 (2019) 70901-70909.

[8] Kumar A., Prajesh R., The Potential of Acoustic Wave Devices for Gas Sensing Applications, Sens. Actuator A-Phys. Physical, 339 (2022) 113498.

[9] Hekiem N.L.L., Ralib A.A.M., Hattar M.A. bt M., Ahmad F., Nordin A.N., Rahim,R.A., Za'bah,N.F., Advanced vapour sensing materials, Existing and latent to acoustic wave sensors for VOCs detection as the potential exhaled breath biomarkers for lung cancer*, Sens. Actuator A-Phys*., 329 (2021) 112792.

[10] Wang Y., Wang,., Liu, W., Chen D., Wu C., Xie J., An aerosol sensor for PM1 concentration detection based on 3D printed virtual impactor and SAW sensor, *Sens. Actuator A-Phys.,* 288 (2019) 67-74.

[11] Zhang X.-F., Zhang Z.-W., He Y.-L., Liu Y.-X., L, S., Fang J.-Y., Zhang X.-A., Peng G., Sniffing lung cancer related biomarkers using an oxidized graphene SAW sensor *Frontiers of Physics*, 11 (2015) 2.

[12] Kidakova A., Borozнjak R., Reut J., Öpik A., Saarma M., Syritski V., Molecularly imprinted polymer-based SAW sensor for label-free detection of cerebral dopamine neurotrophic factor protein, *Sens. Actuator B-Chem.,* 308 (2020) 127708.

[13] Kushwaha M.S., Halevi P., Martínez G., Dobrzynski L., Djafari-Rouhani, B., Theory of acoustic band structure of periodic elastic composites *Phys. Rev. B*, 49 (4) (1994) 2313-2322.

[14] Sigalas M., Economou, E.N., Band structure of elastic waves in two dimensional systems, *Solid State Commun*., 86 (3) (1993) 141-143.

[15] Mead D.M., Wave Propagatıon In Contınuous Perıodıc Structures, Research Contrıbutıons From Southampton, 1964–1995*, J.Sound Vibr.,* 190 (3) (1996) 495-524.

[16] Kushwaha M.S., Halevi P., Dobrzynski L., Djafari-Rouhani B., Acoustic band structure of periodic elastic composites, *Phys.Rev. Lett.,* 71 (13) (1993) 2022-2025.

[17] Achaoui Y., Khelif A., Benchabane S., Robert L., Laude V., Experimental observation of locally-resonant and Bragg band gaps for surface guided waves in a phononic crystal of pillars, *Phys. Rev*. B, 83 (10) (2011) 104201.

[18] Achaoui Y., Laude V., Benchabane S., Khelif A., Local resonances in phononic crystals and in random arrangements of pillars on a surface, *J. Appl. Phys* .114 (10) (2013) 104503.

[19] Jin Y., Pennec Y., Bonello B., Honarvar H., Dobrzynski L., Djafari-Rouhani B., Hussein M.I., Physics of surface vibrational resonances, pillared phononic crystals, metamaterials, and metasurfaces, *Rep. Prog. Phys*., 84 (8) (2021) 086502.

[20] Vasseur J.O., Hladky-Hennion A.-C., Djafari-Rouhani B., Duval F., Dubus,B., Pennec Y., Deymier P.A., Waveguiding in two-dimensional piezoelectric phononic crystal plates, *J. Appl. Phys*., 101 (11) (2007) 114904.

[21] Oh J.H., Lee I.K., M, P.S., Kim Y.Y., Active wave-guiding of piezoelectric phononic crystals, Appl. Phys. Lett., 99(8) (2011) 083505.

[22] Zhang Z.-D., Liu F.-K., Yu S.-Y., Lu M.-H, Chen Y.-F., An integrable and configurable phononic beam splitter based on self-collimated surface acoustic waves, *Appl. Phys. Express*, 13 (4) (2020) 044002.

[23] Schmidt M.-P., Oseev A., Lucklum R., Zubtsov M., Hirsch S., SAW based phononic crystal sensor, technological challenges and solutions, *Microsyst. Technol*., 22 (7) (2016) 1593-1599.

[24] Gharibi H., Khaligh A., Bahrami A., Ghavifekr H.B., A very high sensitive interferometric phononic crystal liquid sensor*, J. Mol. Liq.,* 296 (2019) 111878.

[25] Gharibi H.,Mehaney A., Two-dimensional phononic crystal sensor for volumetric detection of hydrogen peroxide (H2O2) in liquids*, Phys. E Low-dimensional Syst. Nanostructures,* 126 (2021) 114429.

[26] Cao D., Hu W., Gao Y., Guo X., Vibration and energy harvesting performance of a piezoelectric phononic crystal beam*, Smart Mater. Struct*., 28 (8) (2019) 085014.

[27] Bourquin Y., Wilson R., Zhang Y., Reboud J.,Cooper J.M., Phononic Crystals for Shaping Fluids*, Adv. Mater*., 23 (12) (2011) 1458-1462.

[28] Ash B.J., Worsfold S.R., Vukusic P.,Nash G.R., A highly attenuating and frequency tailorable annular hole phononic crystal for surface acoustic waves, *Nature Communications,* 8 (1) (2017) 174.

[29] Ozgur Y., Birol O., Dong X., Srinivas S., Conicity and depth effects on the optical transmission of lithium niobate photonic crystals patterned by focused ion beam, *Opt. Mater. Express*, 1 (7) (2011) 1262-1271.

[30] Levy M., Bass H., Stern R., Modern Acoustical Techniques for the Measurement of Mechanical Properties, *Elsevier Science*, (2001).

[31] Laurell T., Lenshof A., Microscale Acoustofluidics, *Royal Society of Chemistry,* (2014).

[32] Berenge, J.-P., Perfectly matched layer for the FDTD solution of wave-structure interaction problems*, IEEE T. Antenn. Propag.,* 44 (1) (1996) 110-117.

[33] Pennec Y., Djafari-Rouhani B., Larabi H., Vasseur J.O., Hladky-Hennion A.C., Low-frequency gaps in a phononic crystal constituted of cylindrical dots deposited on a thin homogeneous plate, *Phys. Rev. B,* 78 (10) (2008) 104105.